Tuning the flat band with in-plane biaxial strain and the emergence of superconductivity in Ni_3Sn

Hye Jung Kim [1], Min Jae Kim [1], Jaekwang Lee [1], Jong Mok Ok [1,*] and Chang-Jong Kang [2,†]
[1] *Department of Physics, Pusan National University, Busan 46241, Republic of Korea*
[2] *Department of Physics, Chungnam National University, Daejeon 34134, Republic of Korea*

(Received 7 February 2024; revised 7 June 2024; accepted 24 June 2024; published 8 July 2024)

We study the electronic band structures and topological properties of nonmagnetic kagome metal Ni_3Sn when applying in-plane biaxial strains through first-principles calculations. From these calculations, we confirm that the flat band of Ni_3Sn is located at 250 meV below the Fermi level for pristine Ni_3Sn, and its position can be raised to the Fermi level by applying a finite in-plane biaxial strain. In this deformation process, we also find that there are two distinct topological phase transitions between trivial and nontrivial topological states at 1.5% and 2.9% strains. Finally, through the calculations of electron-phonon coupling, we examine the possibility of superconductivity mediated by electron-phonon coupling for pristine and strained Ni_3Sn structures and confirm theoretically that the 5% biaxial strained Ni_3Sn shows superconductivity. Therefore, biaxial strain in kagome metal Ni_3Sn triggers the flat band to move toward the Fermi level, thereby inducing nontrivial topology and superconductivity simultaneously.

DOI: 10.1103/PhysRevB.110.024504

I. INTRODUCTION

Flat-band (FB) materials have attracted much attention as a platform for various novel quantum states such as spin liquids, spin or charge density waves, and superconductivity [1–3]. The FB indicates a dispersionless energy band in momentum space. Due to the quenched kinetic energy, the electronic state of electrons in the FB is spatially localized and the dominant correlation effect between electrons can lead to unusual phenomena [4]. In real materials, nearly flat bands are discovered in two-dimensional (2D) and quasi-2D systems including kagome [2,5–7] and Lieb [8–10] lattices, and three-dimensional (3D) systems including pyrochlore lattices such as $CaNi_2$ and $Ca(Rh_{1-x}Ru_x)_2$ [11]. The nearly flat bands are also realized in the moiré superlattice systems composed of misaligned 2D layers. In particular, the twisted multilayer graphene has attracted attention due to its unconventional superconductivity at specific twist angles [12,13].

The kagome lattice is one of the most typical frustrated lattices with destructive interference. Due to the unique geometry of the lattice structure, it has a special electronic band structure with Dirac bands and FBs [3]. Because of this unique electronic band structure, the various topological states and exotic physical properties theoretically predicted and are also experimentally realized in kagome lattice compounds such as ferromagnetic Fe_3Sn_2 [5], antiferromagnetic FeSn [14], noncollinear antiferromagnetic Mn_3X (X = Sn, Ge) [15], and superconducting AV_3Sb_5 (A = K, Rb, Cs) [16,17]. Due to their exotic properties they have received a lot of attention as candidates for electronic and spintronic applications.

One of the current research interests in kagome materials focuses on how to tune a FB close to the E_F, as the FB is usually rather distant from the E_F. This is important because when the FB is near or at the E_F, emergent physical phenomena such as superconductivity or magnetism can arise, thereby enhancing the intrigue of the system. A recent experiment reported that the FB in $Ca(Rh_{1-x}Ru_x)_2$ could be tuned to the E_F through adjusting the chemical composition ($x = 0.02$), resulting in the appearance of superconductivity with a critical temperature of 6.2 K [11].

From this perspective, we investigate the electronic band structure and topological properties of the nonmagnetic kagome metal Ni_3Sn under in-plane biaxial tensile strains using first-principles calculations. We anticipate that the biaxial strain, typically more efficient and straightforward compared to adjusting the chemical composition, can effectively tune the FB to the E_F in the kagome system of Ni_3Sn. Therefore, our work introduces an alternative method for achieving band alignment through biaxial strain. It is worth noting that recent reports [18,19] on another Ni-based intermetallic kagome compound, Ni_3In, suggest the possible presence of a FB near the E_F, which has sparked renewed interest in Ni-based intermetallic kagome compounds.

In this paper, through electronic band structure calculations and analysis of Z_2 invariants for both pristine and strained Ni_3Sn structures, we examine the energy positions of flat bands and topological properties as a function of the applied strain. We also explore the possibility of superconductivity mediated by electron-phonon coupling (EPC) under the applied strain. We find that as the flat band moves toward the E_F under in-plane biaxial strain, the dominant E_{2g} phonon mode has lower phonon frequency. This substantially boosts the strength of the EPC constant, leading to the onset of superconductivity with distinctive topological features.

*Contact author: okjongmok@pusan.ac.kr
†Contact author: cjkang87@cnu.ac.kr

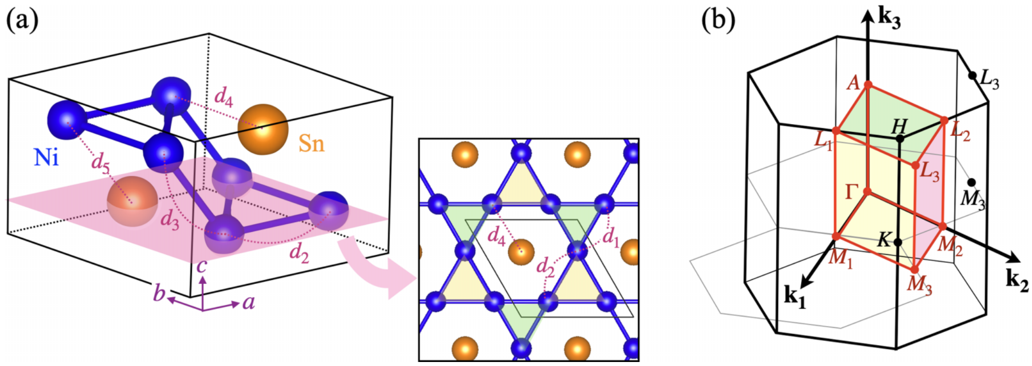

FIG. 1. Crystal structure and Brillouin zone of Ni_3Sn. (a) Crystal structure and (b) Brillouin zone (BZ) of hexagonal Ni_3Sn, consisting of two breathing kagome layers. The inset of (a) shows the atomic arrangement on the red plane indicated in (a). The Ni and Sn atoms are shown as blue and orange spheres, respectively.

II. COMPUTATIONAL DETAILS

Electronic structure calculations were performed within the framework of density functional theory (DFT) utilizing the Vienna *Ab Initio* Simulation Package (VASP) [20,21]. The projector-augmented wave method [22] was employed with a cutoff energy of 400 eV. The generalized gradient approximation (GGA) was adapted for the exchange-correlation functional. Fully structural relaxation was performed until all forces acting on atoms in the unit cell were smaller than 0.001 eV/Å on a $13 \times 13 \times 15$ k mesh. Irreducible representations of bulk electronic states and the surface states band dispersion calculations were done using the IRVSP [23] and WANNIERTOOLS [24] programs, respectively.

Phonon dispersions and electron-phonon coupling calculations were computed using the linear response method [25] implemented in QUANTUM ESPRESSO [26,27]. Electronic wave functions were expanded in plane-wave basis sets with a kinetic energy cutoff of 150 Ry. Standard solid-state pseudopotentials (SSSPs) were used for the calculations [28]. A $12 \times 12 \times 12$ k mesh and $4 \times 4 \times 4$ q mesh were used for phonon calculations, and a $24 \times 24 \times 24$ k mesh for the electron-phonon coupling calculations. The superconducting transition temperatures were obtained using the Allen-Dynes formula [29].

III. RESULTS AND DISCUSSION

A. Crystal structure of Ni_3Sn

The kagome lattice system of Ni_3Sn has a hexagonal structure with the space group $P6_3/mmc$ (No. 194). It consists of Ni_3Sn kagome layers stacked in an AB sequence along the c axis, as illustrated in Fig. 1(a). Structural relaxation calculations yield optimized lattice parameters of $a = b = 5.31$ Å and $c = 4.26$ Å, which agree with a recent experimental result ($a = b = 5.30$ Å and $c = 4.25$ Å) obtained from x-ray diffraction pattern analysis of a single Ni_3Sn crystal [30]. The distances between adjacent Ni atoms (d_1, d_2, and d_3), and between adjacent Ni and Sn atoms (d_4 and d_5), as demonstrated in Fig. 1(a), are determined to be 2.54, 2.77, 2.58, 2.65, and 2.66 Å, respectively. Notably, the sizes of the two triangles filled with yellow and green in a kagome layer [Fig. 1(a)] differ ($d_1 < d_2$), resulting in a breathing kagome lattice structure [31].

B. Electronic structure of Ni_3Sn under in-plane biaxial tensile strain

Figures 2(a)–2(c) show the electronic band structures with spin-orbit coupling (SOC) for pristine Ni_3Sn and two different sizes of in-plane biaxial tensile strain (2% and 5%), respectively. In these biaxial strain deformations, the c/a ratio is altered while maintaining a constant unit-cell volume. An in-plane biaxial tensile strain can be realized through various experimental methods [32,33]. Specifically, it is possible to achieve a biaxial tensile strain of more than 5% using a diamond anvil cell, which can apply uniaxial stress by controlling the pressure medium [34,35]. The bottom of Fig. 2 shows orbital-projected band dispersions within the energy window range of −0.5 to 0.5 eV for each in-plane biaxial tensile strain. It clearly demonstrates that the FB located at ∼250 meV below E_F along Γ-M-K-Γ has dominant Ni by d_{yz}/d_{xz} orbital characters in the pristine structure. This FB arises from destructive interference resulting from the antibonding nature of the wave function trapped in hexagonal plaquettes [11,18]. It also exhibits significant dispersion along the Γ-A line due to considerable overlapping between the interlayer Ni d_{yz}/d_{xz} orbital lobes [18]. Notably, the FB moves toward E_F upon in-plane biaxial tensile strain, as shown in Figs. 2(b) and 2(c). This is significant because the tuning of the FB toward E_F was previously accomplished through chemical tuning in an experiment [11]. Our work provides an alternative method for tuning the position of the FB toward E_F. For 5% tensile strained structure, the FB lies on E_F and intersects with the lowest conduction band, forming a small crossing band gap induced by SOC, as shown in Fig. 2(c).

Since the system possesses both time-reversal and inversion symmetries, which are still conserved under the applied strains, all bands exhibit Kramers degeneracy. The blue shaded region in Fig. 2 represents the energy gap between the lowest conduction and the highest valence bands, resulting in partially filled conduction and valence bands, indicating a semimetallic nature. In the case of pristine Ni_3Sn, along

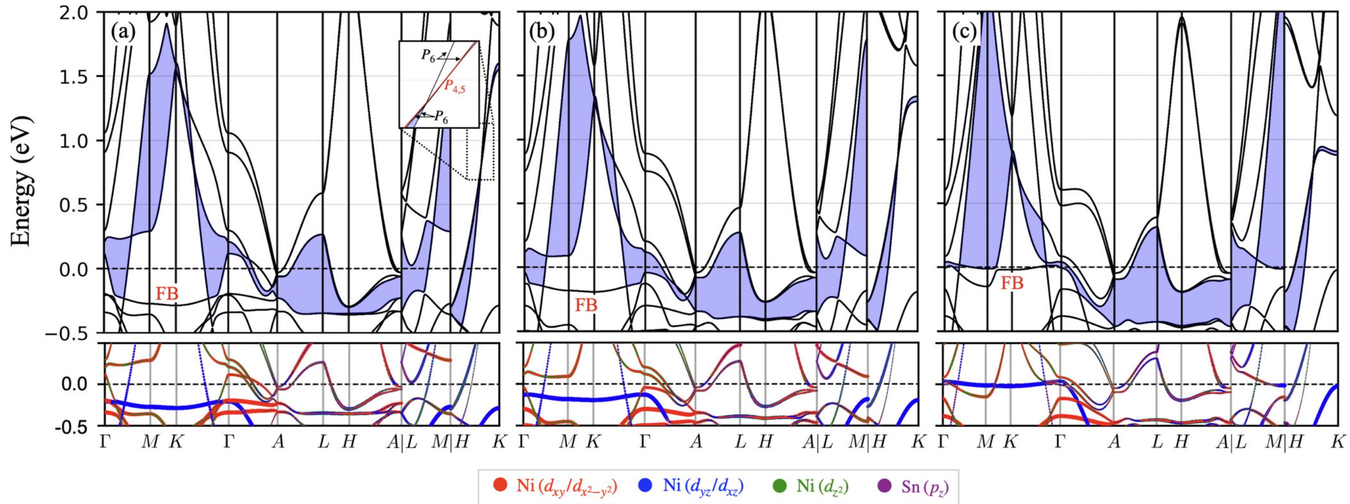

FIG. 2. Electronic band structures of the in-plane biaxial strained Ni_3Sn. Electronic band structures along high-symmetry lines including spin-orbit coupling (SOC) for (a) pristine, (b) 2% strained, and (c) 5% strained Ni_3Sn, respectively. The dashed lines are Fermi level, and the blue shaded regions indicate the energy gap between the lowest conduction and the highest valence bands. In the bottom, we also show the orbital-projected results of bands in the range between −0.5 and 0.5 eV.

the *H*-*K* line, the fourfold degenerate line segment between the lowest conduction and highest valence bands is not split by the SOC, while the other bands near the E_F are slightly split (see Fig. S1 in the Supplemental Material [36]). The inset in Fig. 2(a) illustrates the crossings between bands with P_4, P_5, and P_6 irreducible representations, protected by C_{3z} symmetry, where P_4, P_5, and P_6 have C_{3z} eigenvalues of −1, −1, and 1, respectively. Hence, the crossing is protected by the crystal symmetry of C_{3z} and remains robust under the in-plane tensile strain, as long as the crystal symmetry of C_{3z} is not broken.

C. Electronic topological phase transition under in-plane biaxial tensile strain

To investigate the topological properties of Ni_3Sn, we compute the parity products of the occupied states at time-reversal invariant momentum (TRIM) points and Z_2 invariants [37,38]. In a 3D hexagonal structure, there are eight TRIM points in the Brillouin zone (BZ) labeled as Γ, *A*, three *M* (M_1, M_2, and M_3), and three *L* (L_1, L_2, and L_3), as shown in Fig. 1(b). The four Z_2 invariants (ν_0; $\nu_1\nu_2\nu_3$) are determined as $(-1)^{\nu_0} = \prod_{i=1}^{8}\delta_i$, which is the product over all eight TRIM points; $(-1)^{\nu_1} = \delta_{M_1}\delta_{M_3}\delta_{L_1}\delta_{L_3}$, $(-1)^{\nu_2} = \delta_{M_2}\delta_{M_3}\delta_{L_2}\delta_{L_3}$, $(-1)^{\nu_3} = \delta_A\delta_{L_1}\delta_{L_2}\delta_{L_3}$, respectively. Here, δ_i represents the parity product of the occupied states at a given TRIM point *i*. From the calculations, we obtain nontrivial ($Z_2 = \nu_0 = 1$) for pristine and 5% strained structures, and a trivial ($Z_2 = 0$) for the 2% strained structure, as listed in Table I. Additionally, we found changes in the parity products at the Γ and *M* points induced by the in-plane biaxial strain.

Figures 3(a)–3(d) show the electronic band structures along the *K*-Γ-*M* line and density of states (DOS) of Ni_3Sn under in-plane biaxial tensile strains. As explained previously, the FB approaches the E_F with increasing in-plane biaxial tensile strain. At the strain of 5%, the FB lies on E_F, and a Van Hove singularity occurs at E_F, clearly shown in Fig. 3(d). In the band structure of pristine Ni_3Sn [Fig. 3(a)], the Γ_{12}^- and M_6^- states with negative parity eigenvalues are located above the E_F. As the strain increases, the Γ_{12}^- and M_6^- states shift lower in energy, as indicated by the red and blue dashed lines, respectively, in Figs. 3(a)–3(c). Depending on whether these states are included in the occupied states or not, the parity products at the Γ and *M* points change, as listed in Table I.

Figure 3(e) shows the energy positions of the Γ_{12}^- and M_6^- states as a function of in-plane biaxial strain. Two distinct topological phase transitions are clearly identified at 1.5% and 2.9% strains. Despite efforts to compute the (001) surface states for pristine and two different (2% and 5%) in-plane biaxial tensile strained Ni_3Sn (see Fig. S2 in the Supplemental Material [36]), the surface states are deeply embedded in the bulk states, making it challenging to confirm the presence of topological surface states.

D. Phonon dispersion and superconducting properties of Ni_3Sn

Figures 4(a) and 4(b) show the phonon dispersion curves of pristine and 5% biaxial strained Ni_3Sn structures. In both cases, the phonon frequencies of all modes are positive, indicating the dynamic stability of the metallic kagome system of Ni_3Sn. To examine the possibility of superconductivity mediated by EPC, we compute the EPC constant λ and the

TABLE I. The parity products of the occupied states at TRIM points in the Brillouin zone and Z_2 invariants (ν_0; $\nu_1\nu_2\nu_3$) when applying the in-plane biaxial tensile strain ϵ.

ϵ(%)	Γ	3*M*	*A*	3*L*	(ν_0; $\nu_1\nu_2\nu_3$)
0	−1	+1	−1	−1	(1; 000)
2	+1	+1	−1	−1	(0; 000)
5	+1	−1	−1	−1	(1; 000)

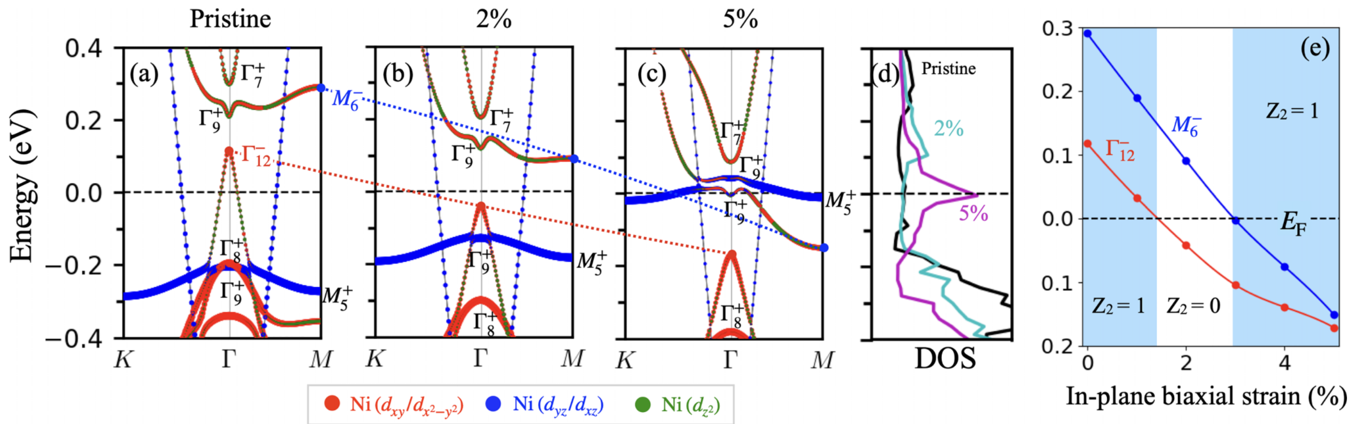

FIG. 3. Tuning the flat bands and topological phase transition of Ni_3Sn by in-plane biaxial strain. (a)–(d) Band structures and density of states (DOS) with SOC when applying the in-plane biaxial tensile strains of 0%, 2%, and 5%, respectively. (e) The change of positions of the Γ_{12}^- and M_6^- states by in-plane biaxial strain. In (a)–(c), the sizes of blue, red, and green filled circles are proportional to the weights of d_{yz}/d_{xz}, d_{xy}/d_{x2-y2}, and d_{z2} orbitals of Ni, respectively. The dashed lines indicate the Fermi level.

superconducting critical temperature T_c. Given that the variations of the electronic structure and the Fermi surface of the system by SOC are small (Figs. S3 and S4 in the Supplemental Material [36]), the SOC effect could be safely neglected in the phonon calculations. According to the Allen-Dynes formula [29,39], the T_c is given by

$$T_c = \frac{\omega_{\log}}{1.2}\exp\left[\frac{-1.04(1+\lambda)}{\lambda-\mu^*(1+0.62\lambda)}\right], \quad (1)$$

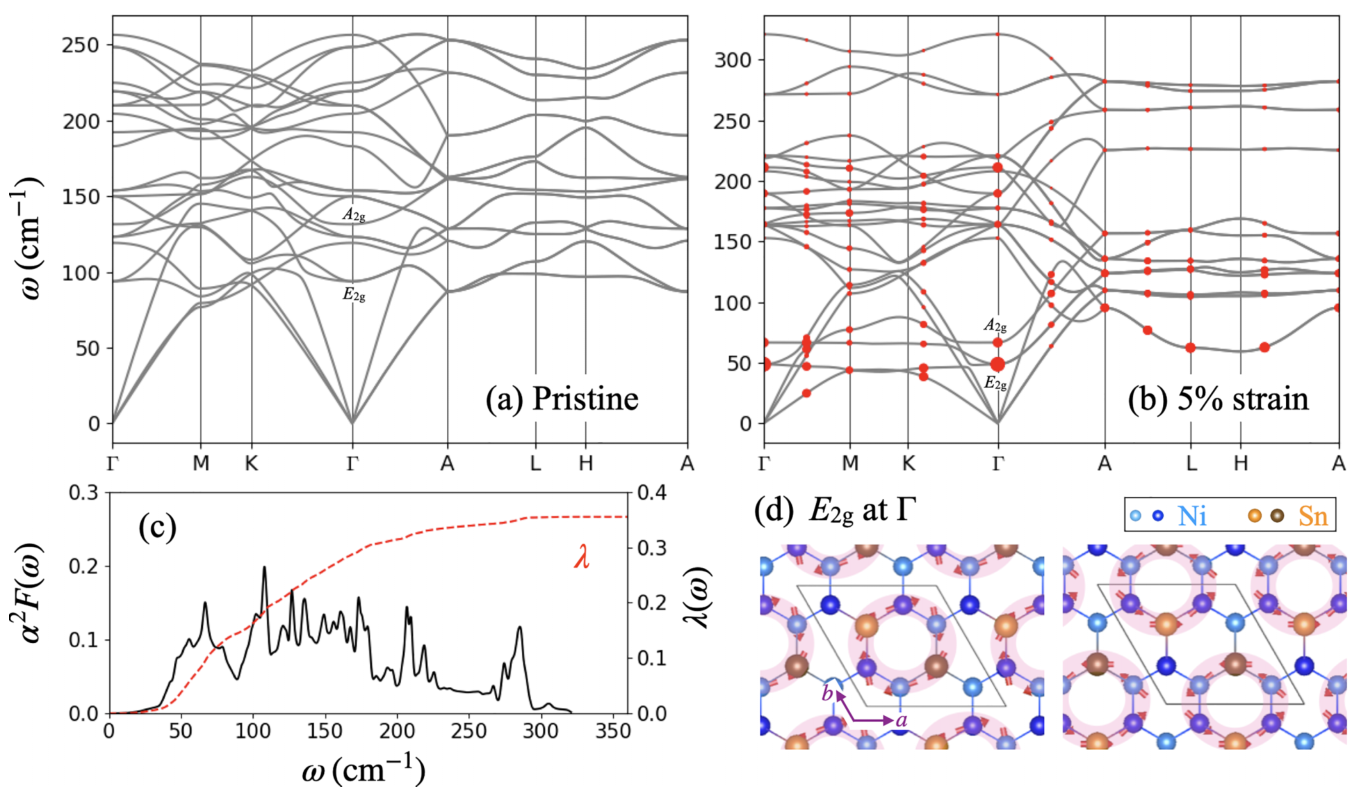

FIG. 4. Electron-phonon coupling (EPC) effect for strained Ni_3Sn. Phonon dispersion curves of (a) pristine and (b) 5% in-plane biaxial strained structures, respectively. In (b), the size of the red filled circles is proportional to EPC strength $\lambda_{\mathbf{q}\nu}$ at phonon wave vector **q** and mode ν. (c) Calculated isotropic Eliashberg spectral function $\alpha^2F(\omega)$ and cumulative EPC $\lambda(\omega)$ for 5% in-plane biaxial strained structure. The red dashed curve is converged to $\lambda = 0.36$. (d) Atomic vibrations of E_{2g} phonon normal mode at the Γ point for 5% strained structure. In this figure, the Ni and Sn atoms in upper (sky blue and orange) and lower (blue and brown) kagome layers are marked with different colors, respectively.

TABLE II. The EPC-related values for pristine and 5% strained Ni_3Sn. Average EPC constant λ, DOS at E_F $N(E_F)$ [states/eV]. The EPC strength $\lambda(E_{2g})$, phonon frequency $\omega(E_{2g})$ [cm^{-1}], and phonon linewidth $\gamma(E_{2g})$ [GHz] are also provided for the E_{2g} phonon mode indicated in Fig. 4.

$\epsilon(\%)$	λ	$N(E_F)$	$\lambda(E_{2g})$	$\omega(E_{2g})$	$\gamma(E_{2g})$
0	0.185	29.775	0.040	93.76	9
5	0.356	62.347	0.158	48.74	20

where μ^* is the effective Coulomb repulsion parameter and $\omega_{\log} = \exp[\frac{2}{\lambda}\int \log\omega \frac{\alpha^2F(\omega)}{\omega}\, d\omega]$ is the logarithmically averaged phonon frequency. From Eq. (1), with a commonly adopted value of $\mu^* = 0.1$ for weakly correlated systems, we obtained that the T_c is 0 for the pristine structure and 0.3 K for the 5% in-plane biaxial strained structure. It could be interpreted that once the FB lies on E_F under 5% strain, it induces electronic instability, thereby leading to the emergence of superconductivity. Even though T_c at the 5% strain is extremely small, it is significantly enhanced compared to the 0% strain case [40]. There is still a possibility that the 5% strain exhibits unconventional superconductivity not explained by the electron-phonon mechanism. In such a scenario, we anticipate that T_c would be much larger than the computed T_c based on the electron-phonon mechanism [41].

To thoroughly investigate its superconducting properties, we explore the EPC strength $\lambda_{\mathbf{q}\nu}$ at the phonon wave vector $\mathbf{q}$ and mode ν for the 5% strained structure. The results are presented as red filled circles in Fig. 4(b). Furthermore, Fig. 4(c) shows the isotropic Eliashberg spectral function $\alpha^2F(\omega)$ and the accumulative EPC $\lambda(\omega)$, formulated by the following expressions [29,42]:

$$\alpha^2F(\omega) = \frac{1}{2}\sum_{\nu}\int_{BZ}\frac{d\mathbf{q}}{\Omega_{BZ}}\,\omega_{\mathbf{q}\nu}\lambda_{\mathbf{q}\nu}\,\delta(\omega-\omega_{\mathbf{q}\nu}), \quad (2)$$

$$\lambda(\omega) = 2\int_0^{\omega}\frac{\alpha^2F(\nu)}{\nu}d\nu. \quad (3)$$

In Fig. 4(c), the computed average EPC constant λ is determined to be 0.36, indicating that the system has relatively weak electron-phonon interactions [29]. At $\omega_0 = 180$ cm^{-1}, the $\lambda(\omega_0)$ is 0.3, representing 83% of $\lambda = 0.36$. The phonon modes between 40 and 180 cm^{-1} contribute the most to the electron-phonon interactions. From the analysis of the EPC strength, $\lambda_{\mathbf{q}\nu}$, as presented in Fig. 4(b), it is evident that the optical E_{2g} phonon normal mode at Γ exhibits a notably significant contribution. The corresponding atomic vibrations associated with this mode are illustrated in Fig. 4(d). The E_{2g} phonon mode is characterized by an in-plane rotational vibration confined within the buckled hexagonal ring as highlighted in the red shaded regions of Fig. 4(d). The FB is significantly influenced by atomic displacements associated with the E_{2g} phonon mode (Fig. S5 in the Supplemental Material [36]), indicating a strong coupling between the FB and the E_{2g} phonon mode. This finding underscores the pronounced influence of the FB and its coupling with the E_{2g} phonon mode, contributing to the enhancement of electron-phonon interactions in the system. Table II shows that DOS at E_F, $N(E_F)$, and the phonon linewidth of the E_{2g} mode, $\gamma(E_{2g})$, under 5% strain increase by 2.1 and 2.2 times, respectively, while the phonon frequency of the E_{2g} mode, $\omega(E_{2g})$, decreases by 0.5 compared to 0% strain. This strain-induced effect is particularly pronounced in enhancing the $\lambda_{\mathbf{q}\nu}$ of the E_{2g} phonon mode, $\lambda(E_{2g})$, which is enhanced by nearly 4.0 times. According to the equation $\lambda(E_{2g}) = \gamma(E_{2g})/\pi N(E_F)\omega(E_{2g})^2$ [43], the enhancement of $\lambda(E_{2g})$ by about 4 times cannot be sufficiently explained by the nearly 2 times enhancements of $N(E_F)$ and $\gamma(E_{2g})$, as these enhancements cancel each other. Instead, the main contribution to enhancement of $\lambda(E_{2g})$ originates from the decrease of the phonon frequency $\omega(E_{2g})$ by 0.5 times. Therefore, the phonon softening of the E_{2g} mode, indicated by the reduction of $\omega(E_{2g})$, is the dominant factor contributing to the enhancement of $\lambda(E_{2g})$. This enhancement of $\lambda(E_{2g})$ subsequently plays a central role in boosting the λ and T_c.

Consequently, the λ value for Ni_3Sn subjected to the 5% in-plane strain significantly surpasses that of pristine Ni_3Sn (1.9 times, Table II). It is estimated that the 5% strain structure has superconductivity at low temperature. This substantial increase suggests the potential of the 5% strained Ni_3Sn as a promising candidate for superconductivity with nontrivial topology.

IV. CONCLUSION

In summary, we have thoroughly investigated the electronic band structure and topological properties of the nonmagnetic kagome metal Ni_3Sn. Through the electronic band structure calculations and analysis of Z_2 invariants, we demonstrate that Ni_3Sn exhibits topological semimetal characteristics with a FB formed by the d_{yz} and d_{xz} orbitals of Ni positioned at 250 meV below the E_F on the Γ-K-M plane. The application of in-plane biaxial tensile strain induces the FB's gradual approach toward the E_F, eventually crossing it at a 5% strain. Notably, during this deformation process, we observe topological phase transitions between trivial ($Z_2 = 0$) and nontrivial ($Z_2 = 1$) topological states at 1.5% and 2.9% strains. Furthermore, through the calculations of EPC along with the Allen-Dynes formula, we estimate the superconducting critical temperature for the 5% strained Ni_3Sn as $T_c = 0.3$ K. We confirm that under in-plane biaxial strain, the movement of the FB toward the E_F, combined with the reduction in phonon frequency of the E_{2g} mode, significantly enhances the EPC strength of the E_{2g} mode, leading to induce superconductivity with nontrivial topology, so-called topological superconductivity. Despite limited experimental studies on Ni_3Sn, our theoretical findings are expected to stimulate further research on this compound in the near future.

ACKNOWLEDGMENTS

C.-J.K. was supported by the National Research Foundation of Korea (NRF) (Grant No. NRF-2022R1C1C1008200). C.-J.K. was also supported by the Korea Institute of Science and Technology Information (KISTI) Supercomputing Center (Projects No. KSC-2022-CRE-0438 and No. KSC-2024-CRE-0050), and the National Research Foundation of Korea Grant funded by the Korean Government (MOE). J.M.O. was supported by the National Research Foundation of

Korea (NRF) grant funded by the Korea government (MSIT) (Grant No. RS-2023-00221154), the 2023 BK21 FOUR Program of Pusan National University, and the Nano & Material Technology Development Program through the National Research Foundation of Korea (NRF) funded by the Ministry of Science and ICT (Grant No. RS-2023-00281839).

[1] S. M. Chan, B. Grémaud, and G. G. Batrouni, Designer flat bands: Topology and enhancement of superconductivity, Phys. Rev. B **106**, 104514 (2022).

[2] M. Kang *et al.*, Topological flat bands in frustrated kagome lattice CoSn, Nat. Commun. **11**, 4004 (2020).

[3] H. Zhang, H. Feng, X. Xu, W. Hao, and Y. Du, Recent progress on 2D kagome magnets: Binary $T_m Sn_n$ ($T =$ Fe, Co, Mn), Adv. Quantum Technol. **4**, 2100073 (2021).

[4] D. Leykam, A. Andreanov, and S. Flach, Artificial flat band systems: From lattice models to experiments, Adv. Phys. X **3**, 1473052 (2018).

[5] Z. Lin, J. H. Choi, Q. Zhang, W. Qin, S. Yi, P. Wang, L. Li, Y. Wang, H. Zhang, Z. Sun *et al.*, Flatbands and emergent ferromagnetic ordering in Fe_3Sn_2 kagome lattices, Phys. Rev. Lett. **121**, 096401 (2018).

[6] Y. Xie *et al.*, Spin excitations in metallic kagome lattice FeSn and CoSn, Commun. Phys. **4**, 240 (2021).

[7] M. M. Denner, R. Thomale, and T. Neupert, Analysis of charge order in the kagome metal AV_3Sb_5($A =$ K, Rb,Cs), Phys. Rev. Lett. **127**, 217601 (2021).

[8] T. Yang, Y. Z. Luo, Z. Wang, T. Zhu, H. Pan, S. Wang, S. P. Lau, Y. P. Feng, and M. Yang, Ag_2S monolayer: An ultrasoft inorganic Lieb lattice, Nanoscale **13**, 14008 (2021).

[9] M. R. Slot, T. S. Gardenier, P. H. Jacobse, G. C. P. van Miert, S. N. Kempkes, S. J. M. Zevenhuizen, C. M. Smith, D. Vanmaekelbergh, and I. Swart, Experimental realization and characterization of an electronic Lieb lattice, Nat. Phys. **13**, 672 (2017).

[10] R. Drost, T. Ojanen, A. Harju, and P. Liljeroth, Topological states in engineered atomic lattices, Nat. Phys. **13**, 668 (2017).

[11] J. P. Wakefield *et al.*, Three-dimensional flat bands in pyrochlore metal $CaNi_2$, Nature (London) **623**, 301 (2023).

[12] Y. Cao, V. Fatemi, S. Fang, K. Watanabe, T. Taniguchi, E. Kaxiras, and P. Jarillo-Herrero, Unconventional superconductivity in magic-angle graphene superlattices, Nature (London) **556**, 43 (2018).

[13] J. M. Park, Y. Cao, K. Watanabe, T. Taniguchi, and P. Jarillo-Herrero, Tunable strongly coupled superconductivity in magic-angle twisted trilayer graphene, Nature (London) **590**, 249 (2021).

[14] M. Kang *et al.*, Dirac fermions and flat bands in the ideal kagome metal FeSn, Nat. Mater. **19**, 163 (2020).

[15] A. Zelenskiy, T. L. Monchesky, M. L. Plumer, and B. W. Southern, Anisotropic magnetic interactions in hexagonal AB-stacked kagome lattice structures: Application to Mn_3X ($X =$ Ge,Sn,Ga) compounds, Phys. Rev. B **103**, 144401 (2021).

[16] Y.-P. Lin and R. M. Nandkishore, Complex charge density waves at Van Hove singularity on hexagonal lattices: Haldane-model phase diagram and potential realization in the kagome metals AV_3Sb_5, Phys. Rev. B **104**, 045122 (2021).

[17] X. Wu *et al.*, Nature of unconventional pairing in the kagome superconductors AV_3Sb_5 ($A =$ K, Rb, Cs), Phys. Rev. Lett. **127**, 177001 (2021).

[18] L. Ye *et al.*, Hopping frustration-induced flat band and strange metallicity in a kagome metal, Nat. Phys. **20**, 610 (2024).

[19] N. Regnault *et al.*, Catalogue of flat-band stoichiometric materials, Nature (London) **603**, 824 (2022).

[20] G. Kresse and J. Furthmüller, Efficiency of *ab-initio* total energy calculations for metals and semiconductors using a plane-wave basis set, Comput. Mater. Sci. **6**, 15 (1996).

[21] G. Kresse and J. Furthmüller, Efficient iterative schemes for *ab initio* total-energy calculations using a plane-wave basis set, Phys. Rev. B **54**, 11169 (1996).

[22] G. Kresse and D. Joubert, From ultrasoft pseudopotentials to the projector augmented-wave method, Phys. Rev. B **59**, 1758 (1999).

[23] J. Gao, Q. Wu, C. Persson, and Z. Wang, IRVSP: To obtain irreducible representations of electronic states in the VASP, Comput. Phys. Commun. **261**, 107760 (2021).

[24] Q. Wu, S. Zhang, H.-F. Song, M. Troyer, and A. A. Soluyanov, WANNIERTOOLS: An open-source software package for novel topological materials, Comput. Phys. Commun. **224**, 405 (2018).

[25] S. Baroni, S. de Gironcoli, A. Dal Corso, and P. Giannozzi, Phonons and related crystal properties from density-functional perturbation theory, Rev. Mod. Phys. **73**, 515 (2001).

[26] P. Giannozzi *et al.*, Advanced capabilities for materials modelling with QUANTUM ESPRESSO, J. Phys.: Condens. Matter **29**, 465901 (2017).

[27] P. Giannozzi *et al.*, QUANTUM ESPRESSO: A modular and open-source software project for quantum simulations of materials, J. Phys.: Condens. Matter **21**, 395502 (2009).

[28] G. Prandini, A. Marrazzo, I. E. Castelli, N. Mounet, and N. Marzari, Precision and efficiency in solid-state pseudopotential calculations, npj Comput. Mater. **4**, 72 (2018).

[29] P. B. Allen and R. C. Dynes, Transition temperature of strong-coupled superconductors reanalyzed, Phys. Rev. B **12**, 905 (1975).

[30] M. Kim *et al.*, Growth of Ni_3Sn single crystal by Czochralski method (unpublished).

[31] A. Bolens and N. Nagaosa, Topological states on the breathing kagome lattice, Phys. Rev. B **99**, 165141 (2019).

[32] J. Liu *et al.*, Controllable strain-driven topological phase transition and dominant surface-state transport in $HfTe_5$, Nat. Commun. **15**, 332 (2024).

[33] E.-J. Guo, R. D. Desautels, D. Keavney, A. Herklotz, T. Z. Ward, M. R. Fitzsimmons, and H. N. Lee, Switchable orbital polarization and magnetization in strained $LaCoO_3$ films, Phys. Rev. Mater. **3**, 014407 (2019).

[34] A. Dewaele and P. Loubeyre, Mechanical properties of tantalum under high pressure, Phys. Rev. B **72**, 134106 (2005).

[35] A. Dewaele, P. Loubeyre, F. Occelli, O. Marie, and M. Mezouar, Toroidal diamond anvil cell for detailed measurements under extreme static pressures, Nat. Commun. **9**, 2913 (2018).

[36] See Supplemental Material at http://link.aps.org/supplemental/10.1103/PhysRevB.110.024504 for comparison of electronic

band structures with and without SOC for pristine Ni_3Sn; (001) surface states for three different in-plane biaxial strained structures; comparison of Fermi surfaces with and without SOC for pristine and 5% strained structures; change of electronic bandstructures due to atomic displacements of the E_{2g} phonon mode for pristine and 5% strained structures.

[37] L. Fu and C. L. Kane, Topological insulators with inversion symmetry, Phys. Rev. B **76**, 045302 (2007).

[38] A. Bansil, H. Lin, and T. Das, Colloquium: Topological band theory, Rev. Mod. Phys. **88**, 021004 (2016).

[39] J. Zhang and G. Q. Huang, The superconductivity and topological surface state of type-II Dirac semimetal $NiTe_2$, J. Phys.: Condens. Matter **32**, 205702 (2020).

[40] The 0% strain case gives $T_c = 0$, which implies no superconductivity, while the 5% strain case yields $T_c = 0.3$ K, suggesting the potential emergence of superconductivity, albeit with a low transition temperature. Note that the computed T_c might not be entirely accurate, as it is based on phonon-mediated conventional theory. Therefore, the T_c computations serve as a guide to determine whether superconductivity may emerge rather than providing an exact value for T_c.

[41] H. Tan, Y. Liu, Z. Wang, and B. Yan, Charge density waves and electronic properties of superconducting kagome metals, Phys. Rev. Lett. **127**, 046401 (2021).

[42] J. Ma, R. Yang, and H. Chen, A large modulation of electron-phonon coupling and an emergent superconducting dome in doped strong ferroelectrics, Nat. Commun. **12**, 2314 (2021).

[43] K. T. Chan, B. D. Malone, and M. L. Cohen, Electron-phonon coupling and superconductivity in arsenic under pressure, Phys. Rev. B **86**, 094515 (2012).